Nano Energy 49 (2018) 209–220

Contents lists available at ScienceDirect

Nano Energy

journal homepage: www.elsevier.com/locate/nanoen

Full paper

Nanoalloy catalysts inside fuel cells: An atomic-level perspective on the functionality by combined *in operando* x-ray spectroscopy and total scattering

Valeri Petkov[a,*], Yazan Maswadeh[a], Yinguang Zhao[b], Aolin Lu[b], Hannah Cronk[b], Fangfang Chang[b], Shiyao Shan[b], Haval Kareem[b], Jin Luo[b], Chuan-Jian Zhong[b], Sarvjit Shastri[c], Peter Kenesei[c]

[a] Department of Physics and Science of Advanced Materials Program, Central Michigan University, Mt. Pleasant, MI 48859, United States
[b] Department of Chemistry, State University of New York at Binghamton, Binghamton, NY 13902, United States
[c] X-ray Science Division, Advanced Photon Source, Argonne National Laboratory, Argonne, IL 60439, United States

ARTICLE INFO

Keywords:
Electrocatalysts for fuel cells
Synchrotron x-ray spectroscopy and total scattering
In operando structure-function studies

ABSTRACT

We introduce an experimental approach for structural characterization of catalysts for fuel cells combining synchrotron x-ray spectroscopy and total scattering. The approach allows probing catalysts inside operating fuel cells with atomic-level precision (~ 0.02 Å) and element specificity (~ 2–3 at%) in both time (~ 1 min) and space (~ μm) resolved manner. The approach is demonstrated on exemplary Pd-Sn and Pt-Ni-Cu nanoalloy catalysts for the oxygen reduction reaction (ORR) deposited on the cathode of an operating proton exchange membrane fuel cell. *In operando* x-ray data show that under operating conditions, the catalyst particles can undergo specific structural changes, ranging from sub-Å atomic fluctuations and sharp nanophase transitions to a gradual strain relaxation and growth, which inflict significant losses in their ORR activity. Though triggered electrochemically, the changes are not driven solely by differences in the reduction potential and surface energy of the metallic species constituting the nanoalloys but also by the formation energy of competing nanophases, mismatch between the size of individual atomic species and their ability to interdiffuse fast in search of energetically favorable configurations. Given their complexity, the changes are difficult to predict and so the resulting ORR losses remain difficult to limit. We show that *in operando* knowledge of the structural evolution of nanoalloy catalysts helps create strategies for improving their activity and stability. In particular, we show that shaping Pd-Sn nanoalloys rich in Pd as cubes reduces the interdiffusion of atoms at their surface and so makes them better catalysts for ORR in fuel cells in comparison to other Pd-Sn nanoalloys. In addition, we demonstrate that the approach introduced here can provide knowledge of other major factors affecting the performance of fuel cells such as operating temperature and the overall catalyst utilization, in particular the evolution of elemental and mass distribution of catalyst particles over the cells' cathode. Last but not least, we discuss how *in operando* x-ray spectroscopy and total x-ray scattering can bridge the knowledge gap between the widely used *in situ* SAXS, EXAFS and monocrystal surface XRD techniques for structural characterization of nanoalloy catalysts explored for energy related applications.

1. Introduction

Fuel cells are a viable alternative to mankind's dependence on fossil fuels. Unfortunately, fuel cells are not on the market yet, mostly because of the lack of efficient and affordable catalysts for the sluggish chemical reactions driving cells' operation, such as the oxygen reduction reaction (ORR). The reaction takes place at the cathode of virtually all fuel cells and, without loss of generality, can be expressed as $O_2 + 4H^+ + 4e^- \rightarrow H_2O$, that is, oxygen molecules adsorbed and reduced at the cell's cathode react with protons supplied by the cell's anode to form water. Studies have shown that the ORR proceeds via a number of steps including, among others, a dissociative adsorption of molecular oxygen and removal of reaction intermediates such as atomic oxygen and hydroxyl (OH) groups. The current understanding is that an efficient catalyst for the ORR would bind oxygen molecules with sufficient strength to facilitate the cleavage of O=O bonds but weakly enough to

* Corresponding author.
E-mail address: petko1vg@cmich.edu (V. Petkov).

https://doi.org/10.1016/j.nanoen.2018.04.049
Received 27 November 2017; Received in revised form 24 March 2018; Accepted 16 April 2018
Available online 18 April 2018

release the reaction intermediates and product when the reaction is complete [1–6].

Pure Pt is the best monometallic catalyst for the ORR, even though, according to theory, it binds oxygen somewhat too strongly by about 0.2 eV [7]. Unfortunately, pure Pt is not suitable for large-scale applications mostly because it is one of the world's scarcest metals. Binary and ternary nanoalloys involving noble metals, such as Pt, Au and Pd, transition metals, such as Ni, Co, Fe and Cu, and post-transition metals, such as Sn and Pb, have proven rather affordable and more active catalysts for the ORR as compared to pure Pt nanoparticles (NPs) [8–12]. Qualitatively, the improvement has been attributed to one or more of the following factors: i) ligand/electronic effects arising from charge exchange between the noble and non-noble metal atoms, ii) strain effects arising from the difference between the size of noble and non-noble metal atoms and iii) geometric effects where particular configurations of surface noble and non-noble metal atoms appear beneficial to the ORR [11–14]. When used inside fuel cells though, the very promising nanoalloy catalysts produced so far are often found less efficient than expected. The reason is that the catalyst particles would undergo specific atomic-level changes that inflict significant losses in their ORR activity, thereby limiting the cells' performance. The problem triggered off a number of studies on the structural transformations of nanoalloy catalysts exposed to the harsh environment inside operating fuel cells, including *in situ* synchrotron SAXS, EXAFS and monocrystal surface XRD [5,9,12,15–19]. Despite extensive research, the driving force, scope and dynamics of the atomic-level changes of functioning nanoalloy catalysts remain not well understood and so the resulting ORR activity losses remain difficult to limit. Here we introduce another synchrotron x-ray radiation based approach for studying catalysts inside fuel cells that combines the proven advantages of energy dispersive x-ray spectroscopy (EDS) and high-energy total x-ray scattering in characterizing nanosized materials at atomic level [20,21]. The great capabilities of the approach are summarized in Scheme 1.

For the sake of generality, we demonstrate the usefulness of the approach by applying it on binary and ternary nanoalloy catalysts involving different noble, transition and post-transition metals. The nanoalloy catalysts probed here have been a subject of *ex situ* studies for ORR activity and stability but never evaluated inside an operating fuel cell. In particular, we study three members of the family of Pd-Sn nanoalloys (with Pd ≥ 50 at%), which have been shown to exhibit both high catalytic activity for the ORR and enhanced tolerance for ethanol and methanol [22]. Largely, the improved ORR activity of Pd-Sn nanoalloys is explained in terms of charge transfer from the less electronegative Sn (1.96) to the more electronegative Pd (2.2.) atoms. The resulting charge-deficient Sn and negatively charged (electron-rich) Pd atoms in the nanoalloys would bind oxygen species stronger and weaker comparing to pure Sn and Pd surfaces, respectively, thereby accelerating the ORR kinetics [23,24]. We also study a catalyst from the family of Pt-Ni-Cu nanoalloys (Pt < 50 at%). Here, the improvement in ORR activity is attributed to charge transfer from the less electronegative transition metal atoms to more electronegative Pt atoms (1.90 for Ni and Cu vs 2.28 for Pt) and, furthermore, shortening of Pt-Pt bonding distances, i.e. compressive strain. The latter is due to the difference in the elemental size of Pt (2.77 Å), Ni (2.50 Å) and Cu (2.56 Å) atoms. Both the charge transfer and compressive strain would lead to a downshift of the *d*-electron band of surface Pt atoms and, hence, diminishing the "poisoning" effect of ORR intermediates. Besides, it is considered that the presence of two types of transition metal atoms in the nanoalloys creates opportunities for manoeuvring of oxygen species over different surface sites, thereby enabling an extra bi-functional mechanism for accelerating the ORR kinetics [9–11,25–27]. Note that according to Pauling's theory of chemical bonding [28], and as shown by independent experimental [29] and DFT studies [30], the length and strength of bonds between atoms in alloys and the exchange of charge between atoms involved in the bonds are strongly coupled. Hence, here we consider that the electronic and strain effects in Pd-Sn and Pt-Ni-Cu nanoalloy catalysts largely act together at atomic level and refer to them as bonding effects. Furthermore, we use the noble metal atom-involving bonding distances as a relative measure of the bonding effects i.e. strength of metal-to-metal atom interactions, in the respective nanoalloys. Lastly, we validate the approach on standard pure Pt and Pt_3Ni catalysts.

2. Experimental

Nanoalloy Pd-Sn and Pt-Ni-Cu particles were synthesized following a wet chemistry route described in the Supplementary information (SI). The as-synthesized NPs were deposited on carbon black and activated for catalytic applications by a post-synthesis treatment involving heating at 260 °C in N_2 for 30 min followed by heating at 400 °C in 15 vol% H_2 for 120 min. The overall chemical composition of activated Pd-Sn and Pt-Ni-Cu alloy NPs, hereafter referred to as fresh Pd-Sn and Pt-Ni-Cu alloy NPs, was determined by inductively coupled plasma atomic emission spectroscopy (ICP-AES) and confirmed by independent EDS as described in the SI. Fresh Pd-Sn alloy NPs appeared with an overall chemical composition of $Pd_{43}Sn_{57}$, $Pd_{78}Sn_{22}$ and $Pd_{95}Sn_5$. The

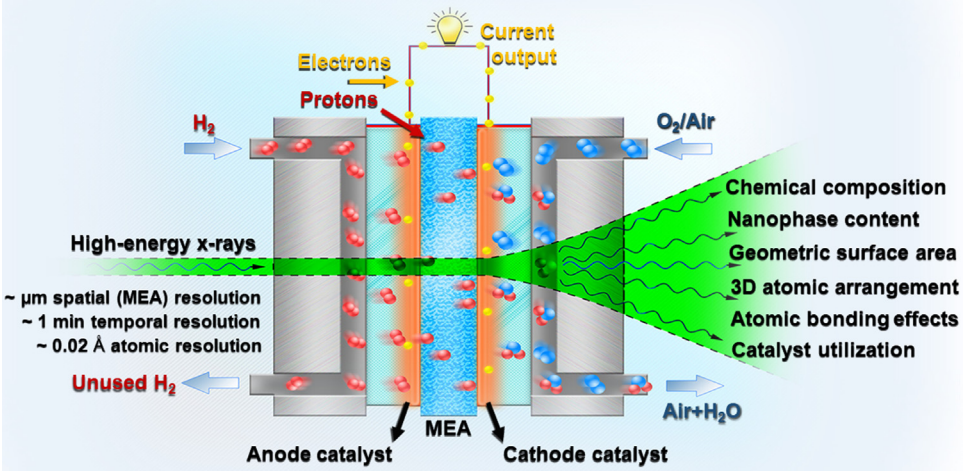

Scheme 1. Mechanistic description of ORR at the cathode of a PEMFC and *in operando* EDS & HE-XRD experiments on the PEMFC cathode catalyst. Hydrogen (H_2) molecules are delivered to the PEMFC anode and split into protons and electrons via a reaction known as the hydrogen oxidation reaction (HOR). The resulting protons permeate through a membrane electrode assembly (MEA) to the PEMFC cathode while electrons reach it via an external circuit, thus generating current output. Oxygen (O_2) molecules reduced at the PEMFC cathode react with the protons arriving at it, forming water. The reaction, known as ORR, is six orders of magnitude slower than HOR, necessitating a very efficient catalyst, e.g. nanoalloy particles, for speeding it up. Thanks to their high-flux and energy, synchrotron x-rays are able to probe the PEMFC cathode catalyst with sub-Å precision, in both time (~ min) and space (~ μm) resolved manner. Experimental data provide information for the evolution of ORR activity, chemical composition, nanophase content, geometric surface area, 3D structure and bonding interactions between the constituent atoms of the PEMFC cathode catalysts as they function under actual operating conditions. The catalysts' utilization, related to the evolving chemistry and mass distribution of the catalysts' particles over the cathode side of MEA, is also assessed.

chemical composition of fresh Pt-Ni-Cu alloy NPs turned out to be $Pt_{37}Ni_{29}Cu_{34}$.

X-ray photoelectron spectroscopy (XPS) measurements described in the SI (see Figs. S18 and S19) confirmed that Pd-Sn particles are nanoalloys wherein the individual Pd and Sn atoms influence each other's electronic structure, including transfer of charge from Sn to Pd atoms. XPS data for $Pt_{37}Ni_{29}Cu_{34}$ alloy NPs indicated a downshift of the occupied *d*-electron states of Pt atoms, likely rendering surface Pt sites in the NPs less reactive in comparison to pure Pt surfaces.

The size and shape of fresh Pd-Sn and Pt-Ni-Cu alloy NPs were determined by Transmission Electron Microscopy (TEM) as described in the SI. Exemplary TEM and high-resolution (HR)-TEM images are shown in Figs. S1 and S2, respectively. As can be seen in the Figures, the NPs are approximately 7.8 (± 1.5) nm in size and spherical in shape. In addition, as indicated by the clear lattice fringes appearing in the respective HR-TEM images, the NPs possess a good degree of crystallinity. The size of fresh NPs was also determined from the full width at the half maximum (FWHM) of strong Bragg-like peaks in their high-energy x-ray diffraction (HE-XRD) patterns. Within the limits of the experimental accuracy, HE-XRD and TEM determined sizes of fresh Pd-Sn and Pt-Ni-Cu alloy NPs appeared about the same.

The catalytic activity of fresh Pd-Sn and Pt-Ni-Cu alloy NPs for the ORR was determined by *ex situ* cyclic voltammetry (CV) and rotating disk electrode (RDE) experiments conducted on a standard 3-electrode cell. The experiments are described in the SI. Results are shown in Fig. S3. As can be seen in the Figure, fresh $Pd_{78}Sn_{22}$ alloy NPs are superior to both fresh $Pd_{43}Sn_{57}$ and $Pd_{95}Sn_5$ alloy NPs in terms of mass activity (MA) for ORR. Upon undergoing 520 potential cycles though, $Pd_{95}Sn_5$ alloy NPs show a significantly increased whereas $Pd_{43}Sn_{67}$ and $Pd_{78}Sn_{22}$ alloy NPs show a greatly decreased ORR activity, respectively. Evidently, upon undergoing electrochemical cycling, $Pd_{95}Sn_5$ alloy NPs acquire a structural state promoting the ORR over their surface. No precise information for the changes of the phase type and content, chemical composition, size and bonding interaction between the constituent atoms of Pd-Sn alloy NPs occurring during the *ex situ* electrochemical cycling though was possible to obtain.

A PEMFC optimized for HE-XRD experiments was used to reveal the atomic-level changes and resulting losses in the ORR activity of Pd-Sn and Pt-Ni-Cu alloy NPs functioning under actual operating conditions. The PEMFC is shown in Fig. S4. Membrane electrode assemblies (MEAs) for the PEMFC were prepared as described in the SI. Following a protocol recommended by DOE [31], the PEMFC was first cycled between 0 V and 1.2 V for about 1 h and then cycled between 0.6 V and 1.0 V for another 5–6 h. The cycling was carried out at 80 °C. In total, the nanoalloys underwent about 1600 potential cycles as deposited on the cathode side of MEAs. During the cycling, high purity hydrogen and nitrogen gas were fed to the PEMFC anode and cathode compartments, respectively. Pure Pt NPs were used as the PEMFC anode catalyst. The current output of the PEMFC was non-stop recorded during the potential cycling. Exemplary polarization curves showing the current output of the PEMFC resulting from the repetitive application of external voltages are shown in Fig. 1c. The curves are typical for accelerated tests for activity and stability of nanoalloy catalysts for ORR (e.g. see Fig. 2 in Ref. [32]). Following the protocol of *ex situ* catalytic studies, values of the MA of Pd-Sn and Pt-Ni-Cu alloy NPs for ORR were obtained from the current output of the PEMFC at 0.9 V on the polarization curves. Rate of changes in the current (in %) with the potential cycling are summarized in Fig. S5. Note that data in Fig. S5 are normalized against the PEMFC current/MA values for the respective fresh, i.e. not cycled NPs. Hence, hereafter, we refer to the data as effective MA activity of cycled Pd-Sn and Pt-Ni-Cu NPs for ORR. As can be seen in the Figure, and in line with the findings of *ex situ* catalytic studies, the ORR activity of cycled $Pd_{43}Sn_{67}$ and $Pd_{78}Sn_{22}$ alloy NPs steadily decreases during the PEMFC operation. On the other hand, after an initial decay, the ORR activity of $Pd_{95}Sn_5$ alloy NPs rebounds a bit and keeps its relatively high value with the further potential cycling.

Atomic-level changes of Pd-Sn and Pt-Ni-Cu nanoalloy catalysts taking place during the PEMFC operation (potential cycling), including changes in their chemistry, geometric surface area, phase content and 3D atomic structure, were probed by EDS and total x-ray scattering coupled to atomic pair distribution function (PDF) analysis. Experiments were done at the 1-ID-C beamline of the Advanced Photon Source at the Argonne National Laboratory using x-rays with energy of 100.2 keV ($\lambda = 0.1236$ Å). Details of the experimental set-up are shown in Fig. S4. HE-XRD patterns were collected in intervals of 1 min throughout the PEMFC operation. Experimental *in operando* HE-XRD patterns for cycled Pd-Sn and Pt-Ni-Co alloy NPs are shown in Fig. S6. As can be seen in the Figure, the patterns exhibit a few strong Bragg-like peaks at low diffraction angles and almost no sharp features at high diffraction angles, i.e. are rather diffuse in nature. The average size of cycled NPs was determined from the FWHM of the strongest Bragg-like peak in the respective HE-XRD patterns using the Scherrer formalism [33]. Results showed that the average size of $Pd_{43}Sn_{57}$, $Pd_{78}Sn_{22}$, $Pd_{95}Sn_5$ and $Pt_{37}Ni_{29}Cu_{34}$ alloy NPs undergone 1600 potential cycles inside the PEMFC increased from 7.8 (± 1.5) nm to about 9.5 (± 1.5) nm, 9.1 (± 1.5) nm, 8.8 (± 1.5) nm and 8.6 (± 1.5) nm, respectively. The so-called geometric surface area (GSA) of nanoalloy catalysts is inversely proportional to the size of nanoalloy particles. In turn, generally, the GSA is proportional to the so-called electrochemical active surface area (ECSA) of the catalysts, which is vital for achieving and maintaining high ORR activity [5,6,31,34,35]. The GSA of Pd-Sn and Pt-Ni-Cu alloy NPs was calculated from the experimental values for the NP size and found to diminish gradually during the PEMFC operation. The rate of change of the GSA, and so of ECSA, of Pd-Sn and Pt-Ni-Cu alloy NPs during the PEMFC operation is shown in Fig. S7. The rather diffuse nature of *in-operando* HE-XRD patterns though prevented applying well-established procedures for in-depth structural characterization of bulk metals and alloys to the nanoalloy particles studied here. Therefore, the patterns were analyzed in terms of atomic pair distribution functions (PDFs) shown in Fig. 2. Details of the derivation of atomic PDFs from HE-XRD patterns can be found in the SI. Here it is to be underlined that experimental total x-ray scattering data, i.e. data comprising both Bragg-like and diffuse x-ray intensities, and so their Fourier counterparts, the atomic PDFs, reflect ensemble-averaged structural features of all metallic alloy NPs sampled by the x-ray beam in a way traditional powder XRD patterns reflect ensemble-averaged structural features of all polycrystalline particles sampled by the x-ray beam in those experiments. Using NP-ensemble averaged structural features to understand and explain NP-ensemble averaged functional properties (e.g. catalytic, magnetic, optical, etc.) puts the exploration of atomic-level structure and properties of metallic alloy NPs on the same footing [36]. EDS spectra for cycled Pd-Sn and Pt-Ni-Cu alloy NPs were taken concurrently with the HE-XRD patterns, that is, in intervals of 1 min. Exemplary EDS spectra are shown in Fig. S8. From the spectra, changes in the overall chemical composition of the NPs during the PEMFC operation were determined following standard procedures [37]. The changes are summarized in Fig. 1a, b and, in better detail, in Fig. S9.

3. Results and discussion

As data in Fig. 1a show, on average, the chemical composition of $Pd_{43}Sn_{57}$, $Pd_{78}Sn_{22}$ and $Pd_{95}Sn_5$ alloy NPs undergone 1600 potential cycles inside the PEMFC has changed to $Pd_{74}Sn_{26}$, $Pd_{65}Sn_{35}$ and $Pd_{81}Sn_{19}$, respectively. Evidently, due to the highly corrosive conditions at the PEMFC cathode, metallic species have leached from the NPs during the PEMFC operation. Based on the differences in the reduction potential (−0.14 V for Sn vs 0.92 V for Pd) and surface energy (0.79 J/m^2 for Sn vs 2.15 J/m^2 for Pd) of Sn and Pd, one may expect that Sn species in cycled Pd-Sn NPs would tend to segregate towards their surface and, furthermore, leach from the NPs in large numbers. Experimental data though show that it is always the majority species that

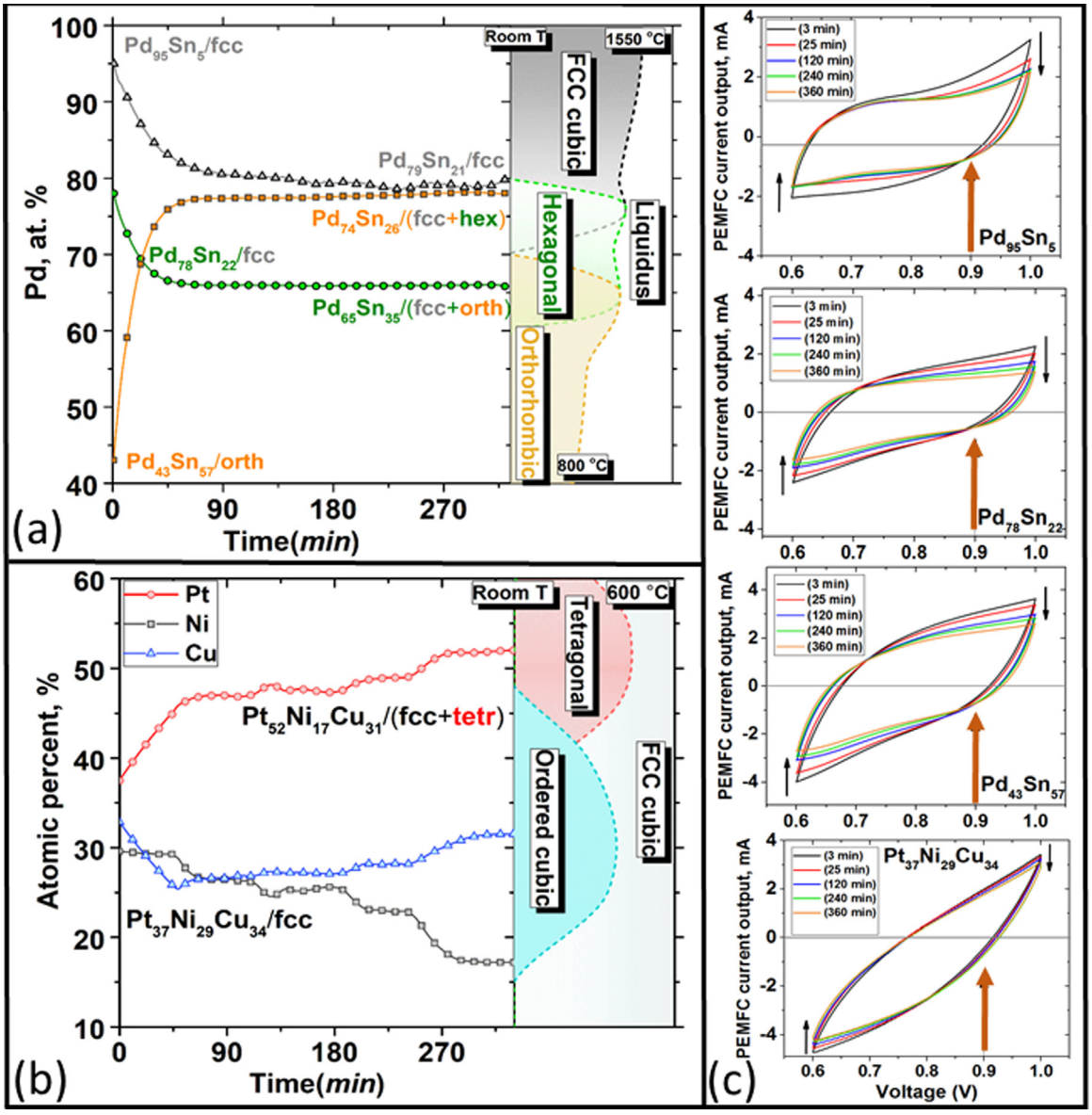

Fig. 1. Evolution of the chemical composition and nanophase type of (a) Pd-Sn and (b) Pt-Ni-Cu NPs during the electrochemical cycling. Phase diagrams of the respective bulk counterparts are shown on the right. (c) Selected polarization curves representing the PEMFC current output recorded during the electrochemical cycling of Pd-Sn and Pt-Ni-Cu NPs in the range from 0.6 V to 1.0 V. The curves tend to collapse, i.e. the PEMFC current output diminishes, during the PEMFC operation (see the thin black arrows on both sides of the curves). Following the protocol of *ex situ* catalytic studies, the current output of the PEMFC at 0.9 V on the polarization curves (follow the thick orange arrows) is used as a measure of the effective MA of Pd-Sn and Pt-Ni-Cu NPs for ORR.

has leached from the respective Pd-Sn NPs. Furthermore, as data in Fig. 2b show, the chemical composition of $Pt_{37}Ni_{29}Cu_{34}$ NPs undergone 1600 potential cycles inside the PEMFC has changed to $Pt_{52}Ni_{17}Cu_{31}$. Here, likely due to their rather low reduction potential (−0.25 V for Ni vs 0.34 V for Cu vs 1.19 V for Pt), minority Ni species have primarily leached from the cycled Pt-Ni-Cu NPs. The observed significant changes in the chemical composition of cycled Pd-Sn and Pt-Ni-Cu alloy NPs prompted us to conduct both qualitative and quantitative (nano)phase analysis of the NPs. The analysis involved a "search and match" procedure based on rigorously comparing atomic PDFs derived from model nanophases with the respective *in operando* PDF data sets. A model reproducing the experimental data in very good detail, i.e. minimizing the residual between the model computed and experimental PDF data set, was considered a truthful representation of the nanophase type and content of the respective NPs. Model nanophases were based on crystal structures adopted by bulk Pd-Sn and Pt-transition metal alloys (transition metal = Ni, Cu). For reference, bulk Pt-(Ni/Cu) and particularly Pd-Sn alloys exhibit a number of intermetallic phases over a broad range of alloys' compositions (see Figs. S10, S11 and S12). Fragments of the phase types explored in the nanophase analysis are shown in Fig. S13. Exemplary results of the nanophase analysis of fresh and cycled Pd-Sn and Pt-Ni-Cu alloy NPs are shown in Figs. 3c, d and 4, S14 and S15. More details of the nanophase analysis can be found in the SI.

As can be seen in Fig. 3d, fresh $Pd_{43}Sn_{57}$ NPs appear as an orthorhombic nanoalloy. Soon after the PEMFC stars operating, that is within the first hour of PEMFC operation, $Pd_{43}Sn_{57}$ NPs suffer big loss in Sn species (see Fig. 1a) and segregate into a mixture of a dominant hexagonal- (87 vol%) and secondary cubic-type (13 vol%) nanophases. After five more hours of potential cycling, the NPs remain phase segregated into a mixture of a hexagonal (79 vol%) and cubic-type (21 vol %) nanophases. As can be seen in Fig. 4, fresh $Pd_{78}Sn_{22}$, $Pd_{95}Sn_5$ and $Pt_{37}Ni_{29}Cu_{34}$ NPs appear as cubic-type nanoalloys. Within the first hour of potential cycling though, $Pd_{78}Sn_{22}$ NPs suffer significant loss in Pd species (see Fig. 1a) and segregate into a mixture of a dominant

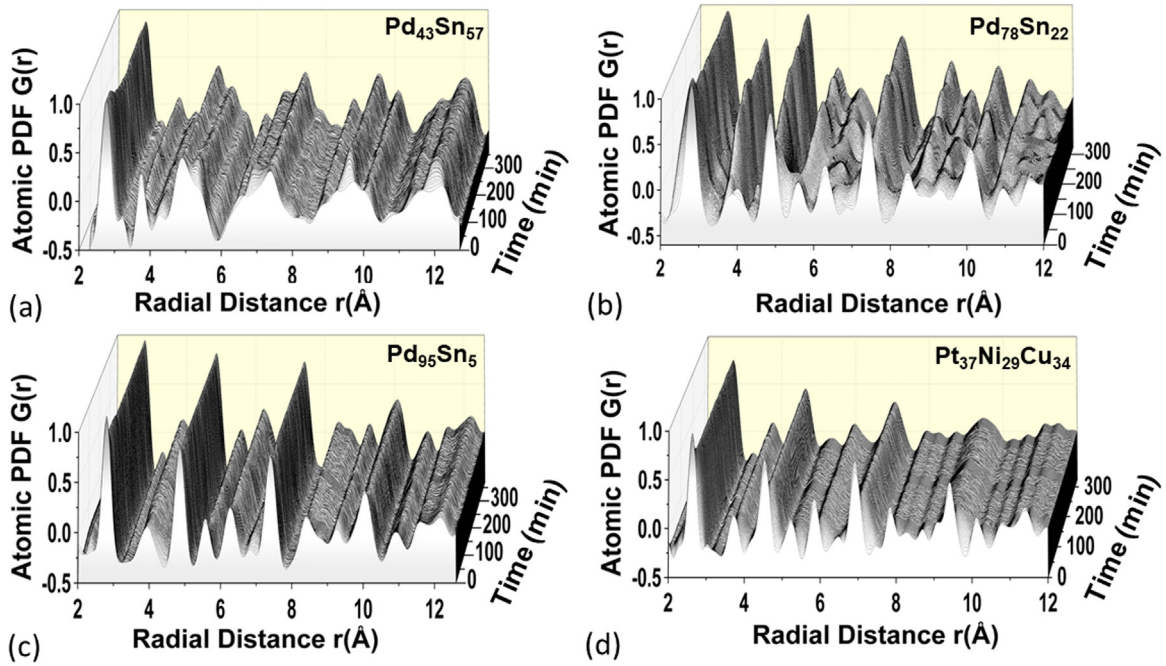

Fig. 2. *In operando* atomic PDFs for Pd-Sn and Pt-Ni-Cu NPs vs time of electrochemical cycling. PDFs are obtained from the HE-XRD patterns shown in Fig. S6.

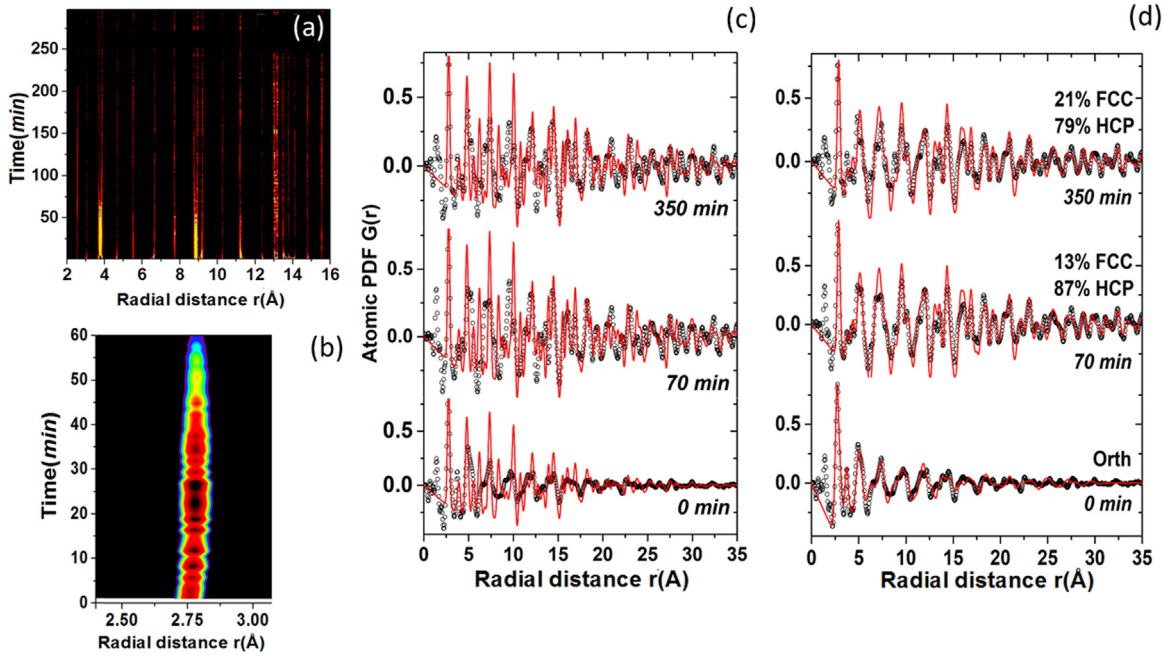

Fig. 3. (a) 2D scedasticity map of the *in operando* atomic PDFs for $Pd_{43}Sn_{57}$ alloy NPs. The map shows that the NPs undergo significant structural changes during the PEMFC operation. Among others, the changes include a relatively sharp nanophase transition (thick bright spots) and continuous readjustment of atomic-pair distances/strain relaxation (thin vertical lines). (b) Color map of the first peak in the *in operando* atomic PDFs for $Pd_{43}Sn_{57}$ NPs. The map shows that the structural changes of the NPs also include highly dynamic sub-Å atomic fluctuations likely arising from re-packing of nearby Pd and Sn atoms (see the sequence of bright and dark spots). (c) Exemplary phase analysis for fresh and cycled $Pd_{43}Sn_{57}$ NPs. The time of cycling is given for each data set. The experimental PDF data (symbols) cannot be reproduced by a model (red line) featuring a single phase fcc-type nanoalloy. As shown in (d), fresh $Pd_{43}Sn_{57}$ NPs are indeed an orthorhombic-type nanoalloy whereas cycled $Pd_{43}Sn_{57}$ NPs segregate into a mixture of a majority hexagonal and minority cubic nanophases. Note that per EDS data, the composition of NPs cycled for about 6 h has changes from $Pd_{43}Sn_{57}$ to $Pd_{74}Sn_{26}$ due to leaching of Sn species.

orthorhombic (82 vol%) and secondary cubic-type (12 vol%) nanophases. Upon undergoing 1600 potential cycles, the NPs end up as a mixture of an orthorhombic (74 vol%) and cubic-type (26 vol%) nanophases. Likewise, within the first hour of PEMFC operation, cycled $Pt_{37}Ni_{29}Cu_{34}$ NPs suffer loss in both Cu and Ni metal species (see Fig. 1b) and segregate into a mixture of a tetragonal (44 vol%) and cubic-type (56 vol%) nanophases. During five more hours of potential cycling, the NPs suffer losses mostly in Ni species and remain phase segregated. On the other hand, regardless having suffered significant loss in Pd species (see Fig. 1a), cycled $Pd_{95}Sn_5$ NPs retain their cubic-type phase state throughout the PEMFC operation. Notably, as data in Figs. 1, 3 and 4 show, both the structure type of fresh Pd-Sn and Pt-Ni-

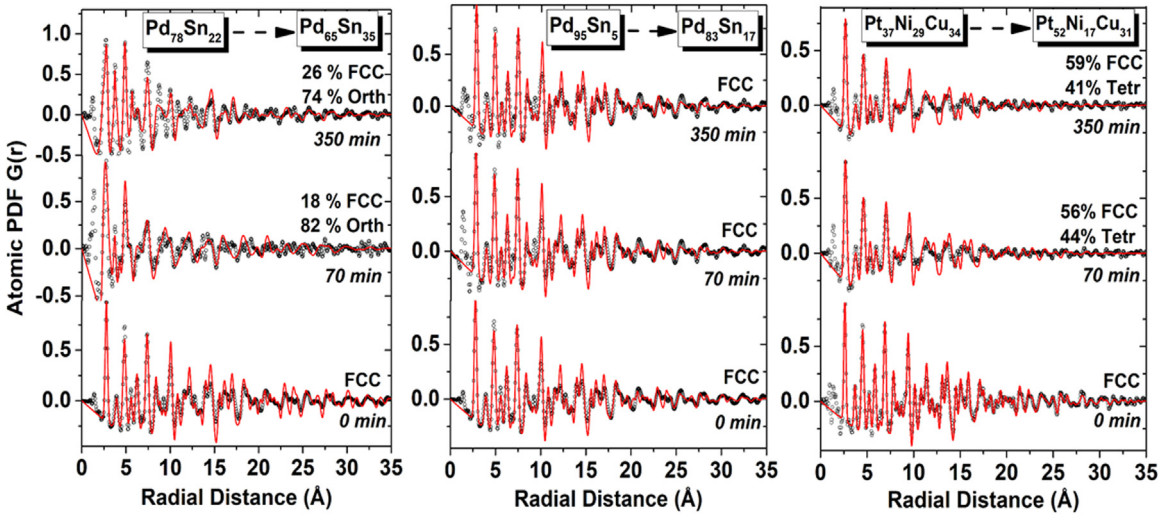

Fig. 4. Nanophase analysis of fresh and cycled $Pd_{78}Sn_{22}$, $Pd_{95}Sn_5$ and $Pt_{37}Ni_{29}Cu_{34}$ alloy NPs. The time of cycling and outcomes of nanophase analysis, including the percentage of individual nanophases in the NPs, are given for each data set. Experimental PDFs (symbols) are matched with computed PDFs (red line) derived from models based on face-centered-cubic (FCC), orthorhombic (Orth) and tetragonal (Tetr) type nanophases. Fragments of the nanophases are given in Fig. S13. Note that, per EDS data, the composition of cycled NPs changes (follow the black arrows in the upper part of the plots) due to leaching of metallic species during the PEMFC operation.

Cu alloy NPs and the trajectory of structural phase transformations they experience during the PEMFC operation mirror the phase diagram of the respective bulk alloys.

Major atomic-level changes in metallic nanoalloy catalysts functioning under real operating conditions, in particular structural nanophase transitions, are seen as big changes in the number, position and intensity of major peaks in the concurrently obtained *in operando* atomic PDFs (e. g. see the PDF data sets for $Pd_{43}Sn_{57}$ NPs shown in Fig. 3c and d). Hence, the changes are easy to recognize by conventionally inspecting the PDFs (e.g. see the color maps of PDF peaks shown in Fig. 3b and S20). Subtle but important atomic-level modifications of functioning nanoalloy catalysts such as, for example, local strain relaxation, may be overshadowed by strong features in the respective PDFs and so are easy to miss. Therefore, we analyzed the *in operando* atomic PDFs for cycled Pd-Sn and Pt-Ni-Cu NPs in terms of the statistical scedasticity formalism. As discussed in the SI, changes in statistical properties of a time series of successive *in operando* PDFs, such as scedasticity, can reveal subtle atomic-level modifications of the studied NPs. 2D scedasticity map computed from the *in operando* PDFs for $Pd_{43}Sn_5$ NPs is shown in Fig. 3a. 2D scedasticity maps for $Pd_{78}Sn_{22}$, $Pd_{95}Sn_5$ and $Pt_{37}Ni_{29}Cu_{34}$ NPs are shown Fig. S20(first row). The maps confirm that cycled Pd-Sn and Pt-Ni-Cu alloy NPs experience major structural changes soon after the PEMFC starts operating. Besides, the maps reveal that the characteristic atomic pair distances and so local strain in the NPs gradually evolve during the PEMFC operation. To be more precise, Pd-involving bonding distances in fresh $Pd_{95}Sn_5$, $Pd_{78}Sn_{22}$ and $Pd_{43}Sn_{57}$ alloy NPs appear expanded by about 1.5%, 1.9% and 4.6%, respectively, as compared to the bonding distance in bulk Pd (2.755 Å). Bonding distances in $Pd_{95}Sn_5$ and $Pd_{78}Sn_{22}$ NPs undergone 1600 cycles appear further expanded, thereby increasing the local tensile strain in the NPs to 1.8% and 2.5%, respectively. Bonding distances in $Pd_{43}Sn_{57}$ NPs undergone 1600 cycles though shrink, diminishing the local tensile strain in the NPs to about 2.9%. When compared to the bonding distance in bulk Pt (2.775 Å), Pt-involving bonding distances in fresh $Pt_{37}Ni_{29}Cu_{34}$ NPs appear compressed by 5.3%. Upon undergoing 1600 potential cycles, the local compressive stain in the NPs diminishes to 3.7%. Markedly, as the oscillations of the intensity of the first peak in the respective *in operando* PDFs show (see the color maps in Fig. 3b, S16 and S20), the structural changes of cycled Pd-Sn and Pt-Ni-Cu NPs also involve frequent sub-Å atomic fluctuations likely related to a re-packing of nearby atoms in the NPs.

The observed continuous changes in the chemical composition and average size of cycled Pd-Sn and Pt-Ni-Cu alloy NPs signal the presence of an effective mass transport within the cathode side of MEA. The magnitude of the mass transport was evaluated by measuring and comparing the elemental and mass distribution (loading) of catalyst particles over the PEMFC cathode for three characteristic time periods of the PEMFC operation. Measurements were done by scanning a 4.5 mm by 4.5 mm area of the MEAs using an x-ray beam with a footprint of about 40 μm by 20 μm. Maps of the elemental and mass distribution of cycled $Pd_{43}Sn_{57}$ alloy NPs over the PEMFC cathode obtained after the PEMFS has operated for about one, two and a half, and five hours are shown in Fig. 5. Maps indicative of the time evolution of the elemental and mass distribution of $Pd_{78}Sn_{22}$, $Pd_{95}Sn_5$ and $Pt_{37}Ni_{29}Cu_{34}$ alloy NPs over the PEMFC cathode are shown in Figs. S21, S22 and S23, respectively. Inspection of the maps reveals that, during the PEMFC operation, catalyst particles accumulate in some and virtually disappear from other *mm*-size areas of the PEMFC cathode. Though to a smaller extent, the average chemical composition of the NPs is also seen to experience *mm*-size fluctuations during the PEMFC operation. Experimental atomic PDFs from spots of the MEAs whereat the loading and chemical composition of the cycled NPs exhibit large fluctuations (follow the slanted arrows in Fig. 5, S21, S22 and S23) are summarized in Figs. S14 and S15. The PDFs are well reproduced by models featuring the nanophases characteristic for the cycled NPs as a whole (compare with the respective data sets shown in Figs. 3 and 4). Results indicate that, largely, it is the loading and average chemical composition and not the phase type of nanoalloy particles that exhibit significant fluctuations over the cathode side of MEA during the PEMFC operation. Altogether, data in Figs. 2–5, S21, S22 and S23 show that, under realistic operating conditions, Pd-Sn and Pt-Ni-Cu alloy NPs undergo significant atomic-level changes, including dissolution of metallic species, sub-Å atomic fluctuations, sharp structural transitions leading to a partial or complete nanophase segregation and local strain relaxation. Besides, the NPs exchange dissolved atomic species over *mm*-range distances and, on average, increase in size by 2–3 nm. Notably, several of the changes occur simultaneously but at significantly different rates.

To quantify the relationship between the atomic-level changes and loss in ORR activity experienced by Pd-Sn and Pt-Ni-Cu alloy NPs during the PEMFC operation, we summarized experimental data for the phase content, GSA and ORR activity of the NPs in Fig. 6. Experimental

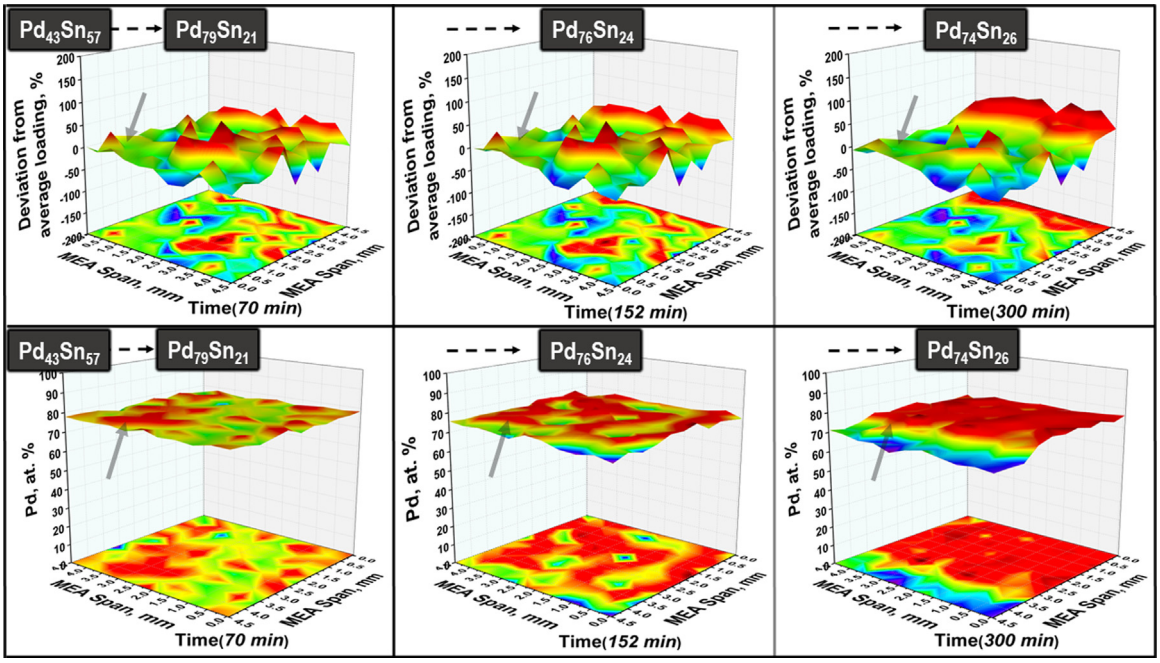

Fig. 5. *(first row)* Mass distribution (loading) of $Pd_{43}Sn_{57}$ nanoalloy particles over a 4.5 mm × 4.5 mm area of the MEA obtained after the PEMFC has operated for 70 min, 152 min and 300 min. The distribution is normalized against the average catalyst loading for that area. (*second row*) Actual percentage of Pd over the same MEA area for the same time periods of the PEMFC operation. Black broken lines connecting black rectangles on top of the plots emphasize the continuously changing average percentage of Pd during the PEMFC operation. Slanted arrows mark MEA's spots whereat the catalyst loading and chemical composition exhibit large fluctuations about the respective average values. Atomic PDFs for the spots are given in Fig. S14. Data are obtained by EDS as described in the SI.

data for the evolution of atomic-level strain in the NPs, as obtained from changes of the respective bonding distances, are also shown in the Figure. As can be seen in the Figure, the ORR activity (effective MA) of both Pd-Sn and Pt-Ni-Cu NPs drops fast soon after the PEMFC starts operating and, furthermore, the magnitude of the drop is different for the different NPs. The drop occurs when the NPs undergo a sharp phase transition and/or the atomic-level strain in the NPs changes fast. It can be rationalized as follows: Based on the difference in the elemental size of Sn (~ 3.2 Å) and Pd (2.75 Å) [38,39], it may be expected that Sn and Pd atoms in Pd-Sn alloy NPs would be under significant “compressive” and “tensile” stress, respectively. It follows then that diminishing the number of majority atoms in the respective NPs, e.g. through dissolution, would be energetically favorable because it would reduce the excessive stress on the minority atoms. Furthermore, Pd and Sn atoms remaining in the nanoalloys would tend to restructure in an energetically favorable configuration. The restructuring would be fast because the interdiffusion of atomic species in nanoalloys is several orders of magnitude faster than that in bulk alloys [40,41]. Besides, it may trigger phase transitions into structure types characteristic of the bulk counterparts of the nanoalloys (see the phase diagram for Pd-Sn system shown Fig. 1a). The local coordination of atoms and bonding distances in the NPs would change accordingly. Concurrent nanophase segregation, changes in the local atomic coordination and bonding distances would disrupt irreversibly cooperative interactions between unlike atomic species in cycled Pd-Sn alloy NPs that are beneficial to the ORR kinetics, in particular the strain and electronic effects discussed above. Hence, the catalytic activity of the NPs for ORR would drop fast, as indeed observed here. The initial trajectory of changes in the atomic structure and ORR activity of cycled Pt-Ni-Cu alloy NPs also appears to be strongly influenced by factors related to minimization of atomic-level stresses and intra-particle diffusion because the NPs are seen to segregate into a mixture of an fcc and not so densely packed tetragonal nanophases (see PDF fits in Fig. 4), both occurring with the respective bulk alloys (see the phase diagram for Pt-TM system shown in Fig. 1b). The gradual diminishing of the ORR activity of both Pd-Sn and Pt-Ni-Cu alloy NPs with the further PEMFC operation coincides with incremental structural changes of the NPs such as a continuous local strain relaxation, variation in the nanophase content and exchange of leached-off metallic species between individual NPs leading to a substantial increase in their size. The concurrent effective mass transport over the PEMFC cathode and likely coalescing of individual NPs can be added to the list. As discussed in work of others [4,6,12,25,42], largely, such structural changes would gradually diminish the ECSA and so overall catalytic activity of the NPs for ORR, which is exactly what our experimental data show. Altogether, data in Fig. 6 indicate the presence of an instant link between the structural changes and ORR activity losses experienced by nanoalloy catalysts functioning inside a PEMFC.

To validate our findings, we studied standard (E-tek) Pt NPs strictly following the experimental protocol described above. Results are summarized in Fig. S25. As can be seen in Figure, Pt NPs cycled for about 5 h suffer a moderate loss in ORR activity, which may be attributed to the combined effect of a local strain relaxation and gradual decrease in their GSA/ECSA. Mass transport over the PEMFC cathode is also moderate in comparison to that observed with Pt-Ni-Cu alloy NPs (compare data in Fig. S23 and S25). Results are in line with the findings of previous studies on the ORR activity and stability of pure Pt NPs [5,12,31,43], thus attesting to the reliability of present *in operando* EDS and total x-rays scattering experiments. We also studied standard Pt_3Ni alloy NPs, which are known to exhibit high ORR activity, this time changing the experimental protocol. In particular, we cycled the NPs for 1 h at room temperature (~ 25 °C) and then for another hour at 80 °C. Results are summarized in Fig. S24 and S26. As can be seen in the Figures, the NPs undergo significant atomic-level changes at room temperature, including loss in Ni species and a concurrent sharp expansion of bonding distances. For reasons discussed above, it may be expected that the ORR activity of the NPs would drop, which is what we observe. An increase in the operating temperature of the PEMFC by 55 °C results in an immediate surge in the current output of the PEMFC (by about 30%). Largely, the surge may be attributed to an improvement of the MEA permittivity [31]. The surge though is likely to be temporary because the catalyst particles keep growing in size and re-

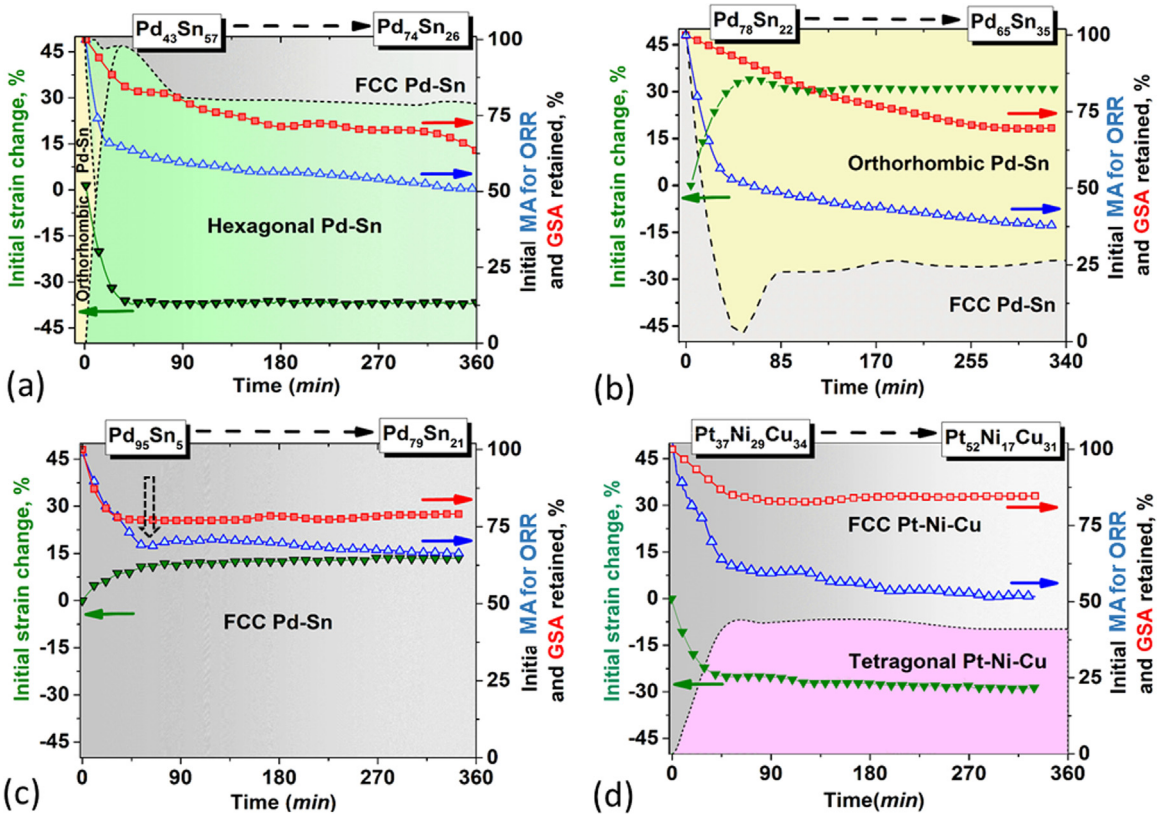

Fig. 6. Color maps of the phase content of (a) $Pd_{43}Sn_{67}$, (b) $Pd_{78}Sn_{22}$, (c) $Pd_{95}Sn_5$ and (d) $Pt_{37}Ni_{29}Cu_{34}$ alloy NPs vs time of electrochemical cycling. Percentage of the individual nanophases are to be read from the vertical axis on the right. The rate of change of the atomic-level strain in the NPs is also given (arrow and symbols in green). For reference, the atomic-level tensile strain in fresh $Pd_{43}Sn_{67}$, $Pd_{78}Sn_{22}$ and $Pd_{95}Sn_5$ alloy NPs is 4.6%, 1.9%, 1.5%, respectively. The atomic-level compressive strain in fresh $Pt_{37}Ni_{29}Cu_{34}$ alloy NPs is 5.3%. As discussed in the text, changes in the atomic-level strain reflect the evolution of bonding distances/effects in the respective NPs. Also given are the retention of the initial GSA (arrow and symbols in red) and effective MA (arrow and symbols in blue) of the NPs for ORR. The former is evaluated from changes in the average NP's size whereas the latter reflects changes in the current output of the PEMFC (e.g. see Fig. 2c). Note that per EDS data, the composition of cycled NPs changes due to leaching of atomic species during the PEMFC operation (follow the horizontal black arrows on top of the plots). Vertical arrow in (c) marks the instant of PEMFC operation when the effective MA of $Pd_{95}Sn_5$ alloy NPs partially recovers from the initial loses and then hardly changes with further cycling.

distributing over the PEMFC cathode. The effect of permanently increased thermal displacements of atoms in the catalyst particles on their ORR activity and, hence, performance of the PEMFCs in terms of current output deserves more detailed structure studies [44]. Nevertheless, results of the experiment involving a Pt_3Ni nanoalloy catalyst for ORR attest to the sensitivity of *in operando* EDS and total x-rays scattering to specifics of the fuel cells' operation. Note that, given the strict temperature, gas flow rate and duty-cycling control exercised during the studies of Pd-Sn and Pt-Ni-Cu alloy NPs, trends exhibited by the data sets presented in Fig. 6 appear highly reliable.

Among others, the *in operando* experiments indicated that the ability of atomic species in nanoalloy particles to interdiffuse fast facilitates structural transformations leading to nanophase segregation and abrupt changes in bonding effects, thus inflicting losses in the nanoalloy's activity for ORR. Here we explored the possibility to bring the interdiffusion under certain control and so reduce the related to it ORR losses by bringing the particle's composition, structure type and morphology in accord with each other. In particular, a comparison between *in operando* (see Fig. S5) and *in house* (see Fig. S3) catalytic data indicated that Pd-Sn alloy NPs with a relatively low Sn content (< 25 at %) and cubic-type atomic structure are potentially excellent catalysts for the ORR taking place inside PEMFCs. Studies of others have also indicated that the optimal surface concentration of the non-noble metal component of binary nanoalloy catalysts for ORR that is capable of providing oxygen species to the NM component, (NM = Pt and Pd), would be in the range of 20–30 at% [45]. Furthermore, the ORR activity of Pd surfaces is known to increase in the order $Pd(110)_{fcc}$ < $Pd(111)_{fcc}$ « $Pd(100)_{fcc}$ [46]. Lastly, it has been demonstrated by experiment that facets generic to structures of metallic atoms tend to stabilize the structures and, hence, their physicochemical properties to a great extent [28,47]. Thus, hinted by the results of present study and work of others, we synthesized Sn-poor nanoalloy particles terminated by $(100)_{fcc}$ facets alone, hereafter referred to as Pd-Sn nanocubes. Details of the synthesis of Pd-Sn nanocubes can be found in the SI. Representative TEM and HR-TEM images of the nanocubes are shown in Fig. 7c and d, respectively. As can be seen in the Figures, the nanocubes appeared with an average size of approximately 7.5 (± 1.5) nm and good crystallinity. Per ICP-AES, the average chemical composition of the nanocubes turned out to be $Pd_{96}Sn_4$. The nanocubes were subjected to an accelerated test for ORR activity and stability following the protocol described above. Analysis of the experimental *in operando* atomic PDFs showed that, regardless having suffered loss in Pd species (~ 15 at % from the initial value; see Fig. S9), the nanocubes maintain their cubic-type atomic structure and bonding distances during the potential

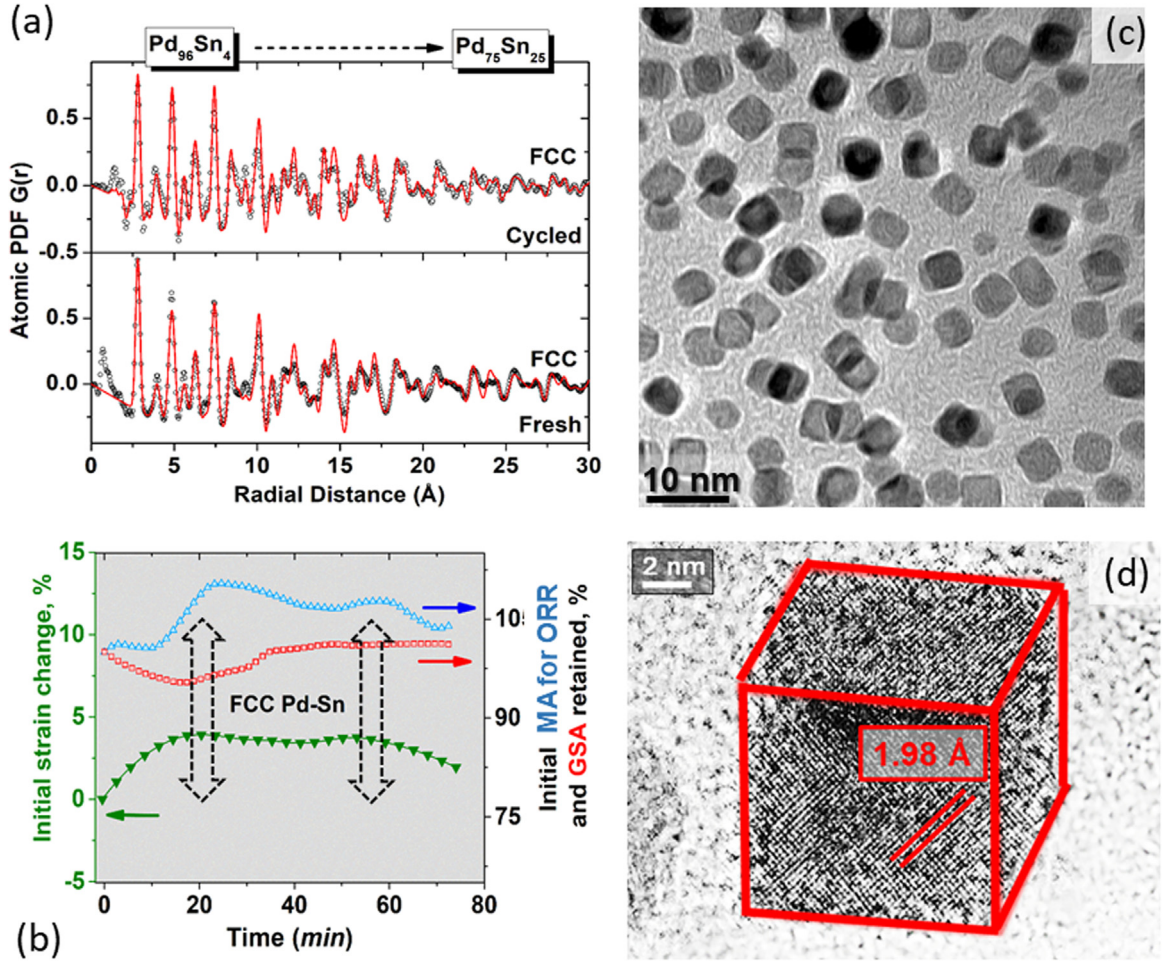

Fig. 7. (a) Exemplary nanophase analysis of fresh and cycled Pd-Sn nanocubes. Note that per EDS data, the composition of nanocubes changes (follow the horizontal arrow on top of the plot) during the PEMFC operation. (b) Rate of change of the atomic-level strain in the nanocubes during the PEMFC operation (symbols and arrow in green). For reference, the tensile atomic-level strain in the fresh nanocubes is + 1.9%. As discussed in the text, changes in the atomic-level strain reflect the evolution of bonding distances/effects in the NPs. Also given are the retention of the initial GSA (symbols and arrow in red) and the effective MA (symbols and arrow in blue) of the nanocubes for ORR. The former is evaluated from changes in the average NP's size whereas the latter reflects changes in the current output of the PEMFC at 0.9 V on the respective polarization curves. Vertical broken lines emphasize the concurrent changes in the bonding distances, GSA and MA of the nanocubes during the PEMFC operation. The oscillatory behavior of bonding distances indicates that the nanocubes adopt some transient structural states of an fcc-type that improve their ORR activity temporarily. (c) TEM image of fresh nanocubes. The nanocubes are with an average size of approximately 7.5 (± 1.5) nm. (d) Representative HR-TEM image for a fresh nanocube. The nanocube has a very regular surface terminated with $(100)_{fcc}$-type facets (see the slanted lines in red). The interplanar $(200)_{fcc}$ distance in the nanocubes is 1.98 Å. It is slightly longer than the $(200)_{fcc}$ distances of 1.945 Å in bulk Pd, confirming that the nanocubes are Pd-Sn nanoalloys.

cycling (see Fig. 7a). The nanocubes do not suffer significant loss in ORR activity either (see Fig. S5). On the contrary, under operating conditions, they adopt transient structural states that exhibit somewhat improved ORR activity (see the slow oscillations in the MA, GSA and strain values summarized in Fig. 7b). We argue that Pd-Sn nanocubes preserve their structural integrity and so ORR activity because the interdiffusion of atoms near their facets is reduced to hopping of atoms between largely equivalent positions. The lack of significant fluctuations in both the position and intensity of the first peak in the *in operando* PDFs for the cycled nanocubes also indicates that they do not experience irreversible structural changes during the PEMFC operation (see Fig. S16). A comparison between the higher-r part of the experimental atomic PDFs for cycled $Pd_{96}Sn_4$ nanocubes and spherical $Pd_{95}Sn_5$ NPs indicates that the surface of the former indeed remains more ordered at atomic level as compared to that of the latter (see Fig. S17). This is important because uneven surfaces of nanoalloys involving Pd are known to bind ORR intermediates stronger than smooth Pd surfaces and so underperform as catalysts for ORR [4–6,18,43]. Currently, we are optimizing the ORR activity of Pd-Sn nanocubes by fine-tuning details in their synthesis and post-synthesis treatment.

It may be difficult to decide '*a priori*' on the relative importance of factors such as reduction potential, surface energy and size of distinct atomic species, propensity to form stable nanostructures through full-scale phase transitions and/or continuous local re-alloying, particle growth and mass redistribution over the cells' cathode in determining the type and scope of atomic-level changes that nanoalloy catalysts would indeed undergo under operating conditions [39]. The experimental approach introduced here may be very helpful in this respect due to its ability to identify the major factors behind the observed ORR activity losses without evoking model assumptions and, hence, enable

the development of a rational strategy for reducing the latter through taking control over the former. Besides, it can bridge the knowledge gap between other widely used *in situ* techniques for atomic-level characterization of nanoalloy catalysts such as *in situ* SAXS, EXAFS and monocrystal surface XRD. In particular, *in situ* SAXS provides valuable information for the evolution of the size and morphology of catalyst particles during potential cycling [1,5,6,48]. Data for the evolution of the particle's structure type obtained by PDF analysis of x-ray scattering data can be used to clarify the findings of SAXS experiments, as exemplified in Ref. [19]. *In situ* EXAFS provides valuable information for the local coordination and valence electronic structure of atoms in nanoalloy catalysts [5,6,15,17]. Structural characteristics of cycled catalyst particles obtained by EDS and total x-ray scattering experiments, in particular chemical composition, nanophase type and degree of local atomic disorder, can help improve the accuracy of EXAFS fitting models [49,50]. *In situ* monocrystal surface XRD provides fundamental knowledge of catalyst surfaces [12,18]. The knowledge can be extended to facets of actual catalyst particles and proven in practice, as demonstrated above.

4. Conclusions

In summary, combined *in operando* x-ray spectroscopy and total scattering experiments conducted here evidence that, under operating conditions, nanoalloy catalysts for the ORR taking place at the cathode of fuel cells, in particular PEMFCs, can undergo structural changes with a largely different dynamics and/or scope. The changes can be identified and quantified with atomic-level precision (~ 0.02 Å) and element specificity (~ 2–3 at%), and linked to the resulting ORR activity losses in both time (~ 1 min) and space (~ μm) resolved manner. This experimental approach expands on the *ex situ* techniques currently in use by providing unique information for the evolution of the chemical composition, geometric surface area, phase content, 3D structure and strength of interactions between the constituent atoms of nanoalloy catalysts functioning under realistic operating conditions, as exemplified in Scheme 1. The overall catalyst utilization, related to the elemental and mass distribution of catalyst particles over the PEMFC cathode, and specifics of the PEMFC's operation such as, for example, operation temperature, can also be assessed. The knowledge can provide valuable feedback on the success of the ongoing effort to engineer better MEAs in particular, and optimize the performance of PEMFCs in general. Ultimately, combined with other widely used *in situ* techniques for structural characterization of functioning catalysts such as *in situ* SAXS, EXAFS and monocrystal surface XRD, *in operando* x-ray spectroscopy and total scattering can help transform the promise of fuel cell technologies into an affordable reality.

Acknowledgments

This work was supported by DOE-BES Grant DE-SC0006877. Also, it used resources of the Advanced Photon Source at the Argonne National Laboratory provided by the DOE Office of Science under Contract No. DE-AC02-06CH11357. Thanks are due to Dr. B. Prasai for the help with HE-XRD experiments.

Notes

The authors declare no competing financial interest.

Appendix A. Supporting information

Supplementary data associated with this article can be found in the online version at http://dx.doi.org/10.1016/j.nanoen.2018.04.049.

References

[1] H.A. Gasteiger, S.S. Kosta, B. Sompalii, F.T. Wagner, Appl. Catal. B 56 (2005) 9.
[2] T. Toda, H. Igarashi, M. Watanabe, J. Electrochem. Soc. 145 (1998) 4185–4188.
[3] L. Chen, H. Guo, T. Fujita, A. Hirata, W. Zhang, A. Inoue, M. Chen, Adv. Funct. Mater. 21 (2010) 4364–4370.
[4] B. Hammer, J.K. Norskov, Adv. Catal. 45 (2007) 71–129.
[5] B.R. Cuenya, F. Behafarid, Surf. Sci. Rep. 70 (2015) 135–187.
[6] E. Antolini, J.R.C. Salgado, E.R. Gonzales, J. Power Sources 16 (2006) 957–968.
[7] L. Bu, N. Zhang, S. Guo, X. Zhang, J. Li, J. Yao, T. Wu, G. Lu, J.-Y. Ma, D. Su, X. Huang, Science 354 (2016) 1410–1414.
[8] Note, following the widely adopted definition (e.g., see: Callister, W. D. Materials Science and Engineering: An Introduction; John Wiley & Sons: New York, 2007), throughout the paper the term “alloy” is used to describe any mixture of distinct metallic species, irrespective of the degree of their mixing and way of mixing
[9] P. Strasser, S. Oh, T. Anniyev, G. Greely, K. More, Ch. Yu, Z. Liu, S. Kaya, D. Nordlund, H. Ogasawara, M.F. Toney, A. Nilsson, Nat. Chem. 2 (2010) 454–460.
[10] X. Huang, Z. Zhao, L. Cao, Yu Chen, E. Zhu, Zh Lin, M. Li, A. Yan, A. Zettl, Y.M. Wang, X. Duan, T. Mueller, Yu Huang, Science 348 (2015) 1230–1234.
[11] V.R. Stamenkovic, B.S. Mun, K.J.J. Mayrhofer, P.N. Ross, N.N. Markovic, J. Am. Chem. Soc. 128 (2006) 8813–8819.
[12] A.F. Pedersen, E.T. Ulrikkeholm, M.-E. Escribano, T.P. Johansson, P. Malacrida, H.M. Pedersen, M.H. Hansen, K.D. Jensen, J. Rossmeisl, D. Friebel d, A. Nilsson, Ib Chorkendorff, I.E.L. Stephens, Nano Energy 29 (2016) 249–260.
[13] M. Mavrikakis, B. Hammer, J.K. Norskov, Phys. Rev. Lett. 13 (1998) 2819–2822.
[14] F. Maroun, F. Ozanam, O.M. Magnussen, R.J. Behm, Science 293 (2001) 1811–1814.
[15] A.I. Frenkel, J.A. Bokhoven, J. Synchrotron Rad. 21 (2014) 1084–1089.
[16] L.R. Merte, F. Behafarid, D.J. Miller, D. Friebel, S. Cho, F. Mbuga, D. Sokaras, R. Alonso-Mori, Tsu-Chien Weng, D. Nordlund, A. Nilson, B.R. Cuenya, ACS Catal. 2 (2012) 2371–2376.
[17] N. Ishiguro, T. Saida, T. Uruga, Shin-ichi Nagamatsu, O. Sekizawa, K. Nitta, T. Yamamoto, Shin-ichi Ohkoshi, Y. Iwasawa, T. Yokoyama, M. Tada, ACS Catal. 2 (2012) 1319–1330.
[18] N.S. Marinkovic, K. Sasaki, R.R. Adzic, Front. Energy 11 (2017) 236–244.
[19] X. Tuaev, S. Rudi, V. Petkov, A. Hoell, P. Strasser, ACS Nano 7 (2013) 5666–5674.
[20] A.A. Herzing, M. Watanabe, J.K. Edwards, M. Conte, Z.-R. Tang, G.J. Hutchings, Ch.J. Kiely, Faraday Discuss. 138 (2008) 337–351.
[21] V. Petkov, L. Yang, J. Yin, R. Loukrakpam, S. Shan, B. Wanjala, J. Luo, K.W. Chapman, C.-J. Zhong, Phys. Rev. Lett. 109 (2012) 125504 (5pp).
[22] M.R. Miah, J. Masud, T. Ohsaka, Electrochem. Acta 56 (2010) 285–290.
[23] S. Salome, A.M. Ferraria, A.M. Botelho do Rego, F. Alcaide, O. Savadogo, R. Rego, Electrochem. Acta 192 (2016) 268–282.
[24] M.R. Miah, M.T. Alam, T. Okajima, T. Ohsaka, J. Electrochem. Soc. 156 (2009) B1142–B1149.
[25] V.R. Stamenkovic, B.S. Mun, M. Arenz, K.J.J. Mayrhofer, C.A. Lucas, G. Wang, P.N. Ross, N.N. Markovic, Nat. Mater. 6 (2007) 241–247.
[26] S. Mukerjee, S. Srinivasan, M.P. Soriaga, J. McBreen, J. Electrochem. Soc. 142 (1995) 1409–1422.
[27] B.N. Wanjala, R. Loukrampam, J. Luo, P.N. Njoki, D. Mott, C.J. Zhong, J. Phys. Chem. 14 (2010) 17580–17590.
[28] L. Pauling, The Nature of the Chemical Bond, Cornell University Press, Ithaca, NY, 1975.
[29] T. Rajasekharan, V. Seshubai, Acta Crystallogr. Sect. A: Found. Crystallogr. 68 (2012) 156–165.
[30] J.R. Kitchin, J.K. Norskov, M.A. Barteau, J.G. Chen, Phys. Rev. Lett. 93 (2004) 156801.
[31] R. Borup, J. Meyers, B. Pivovar, Y.S. Kim, R. Mukundan, N. Garland, D. Myers, M. Wilson, F. Garzon, D. Wood, P. Zelenay, K. More, K. Stroh, T. Zawodzinski, J. Boncella, J.E. McGrath, M. Inaba, K. Miyatake, M. Hori, K. Ota, Z. Ogumi, S. Miyata, A. Nishikata, Z. Siroma, Y. Uchimoto, K. Yasuda, K.-i. Kimijima, N. Iwashita, Chem. Rev. 107 (2007) 3904–3951.
[32] C.A. Rice, Patrick Urchaga, A.O. Pistono, B.W. McFerrin, B.T. McComb, J. Hu, J. Electrochem. Soc. 162 (2015) F1175–F1180.
[33] P.K. Klug, L.E. Alexander, X-Ray Diffraction Procedures: For Polycrystalline and Amorphous Materials, Wiley, 1974.
[34] E.F. Holby, W. Sheng, Y. Shao-Horn, D. Morgan, Environ. Sci. 2 (2009) 865–871.
[35] J.A. Gilbert, N.N. Kariuki, R. Subbaraman, A.J. Kropf, M.C. Smith, E.F. Holby, D. Morgan, D.J. Myers, J. Am. Chem. Soc. 134 (2012) 14823–14833.
[36] V. Petkov, B. Prasai, S. Shastri, H.-U. Park, Y.-U. Kwon, V. Skumryev, Nanoscale 9 (2017) 15505–15514.
[37] D.E. Newbury, Characterization of Materials, Wiley, 2002.
[38] W. Martinssen, H. Warlimont, Condensed Matter and Materials Data, Springer, 2005.
[39] J.K. Norskov, T. Bligaard, J. Bergsma, J. Catal. 209 (2002) 275–278.
[40] H. Yasuda, H. Mori, Phys. Rev. Lett. 69 (1992) 3747–3750.
[41] Q. Zhang, J.Y. Lee, J. Yang, Ch Boothroyd, J. Zhang, Nanotechnology 18 (2007) 245605.
[42] J. Zhang, K. Sasaki, E. Sutter, R.R. Adzic, Science 315 (2007) 220–222.
[43] S. Cherevko, N. Kulyk, K.J.J. Mayrhofer, Nano Energy 29 (2016) 275–298.
[44] F.D. Vila, J.J. Rehr, R.A. Nuzzo, A.I. Frenkel, J. Phys. Chem. Lett. 14 (2017)

3284–3288.
[45] J.L. Fernandes, D.A. Walsh, A.J. Bard, J. Am. Chem. Soc. 127 (2005) 357–365.
[46] M. Shao, T. Yu, J.H. Odell, M. Jin, Y. Xia, ChemComm 47 (2011) 6566–6568.
[47] W.B. Pearson, The Crystal Chemistry and Physics of Metals and Alloys, Wiley-Interscience, 1972.
[48] A. Rabis, P. Roudriguez, Th.J. Schmidt, ACS Catal. 2 (2012) 864–890.
[49] S.T. Chill, R.M. Anderson, D.F. Yancey, A.I. Frenkel, R.M. Crooks, G. Henkelman, ACS Nano 9 (2015) (4036-4032).
[50] J. Timoshenko, A.I. Frenkel, Catal. Today 280 (2017) 274–282.

Valeri Petkov is a Professor in Physics at Central Michigan University. He has over 30 years of research experience in x-ray diffraction studies of materials with intrinsic structural disorder, and more than 180 papers published in peer-reviewed journals.

Yazan Maswadeh is a Ph.D. candidate in the Physics Department at Central Michigan University. He is working with Prof. Petkov's group since 2015 and have contributed to a number of papers published in peer-reviewed journals. His current research interests include structural characterization of nanosized materials using x-ray diffraction and spectroscopy, atomic structure-function relationship, and investigating electrocatalysts functioning inside fuel cells.

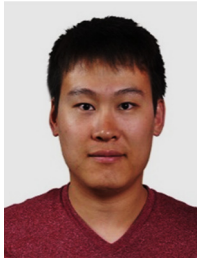

Yinguang Zhao received his MA degree in Chemistry from the State University of New York at Binghamton in 2017. His research project at Binghamton University involved experimental measurements of the phase structures and catalytic activities of nanoalloy catalysts for fuel cell reactions.

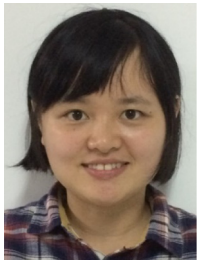

Aolin Lu received her Ph.D. degree in Materials Physics and Chemistry from Xiamen University, China in 2017. She was a visiting Ph.D. student in Prof. Zhong's group at the State university of New York at Binghamton. Currently, she is a Postdoctoral Fellow at Xiamen University. She has co-authored several papers in peer-reviewed journals. Her research interests include nanomaterials, electrochemistry, energy conversion and environmental catalysis.

Hannan Cronk received her Ph.D in Chemistry from the State University of New York at Binghamton in Dec 2017 under the supervision of Prof. Zhong. She started recently her academic career at North Central State College. She has co-authored several publications in peer-reviewed journals. Her research interests include design and synthesis of multimetallic nanoscale materials for clean energy production, conversion and storage applications.

Fangfang Chang received her Ph.D. degree in Chemistry from Hunan University in 2017. Her research interests include nanoscale catalyst synthesis, characterization and application in clean energy conversion technologies such as fuel cells. Part of her Ph.D. work was done at the State University of New York at Binghamton under the supervision of Prof. Zhong. She started recently her academic career at Henan Normal University. She has co-authored a number of peer-reviewed papers on supported nanocatalysts for electrochemical reactions.

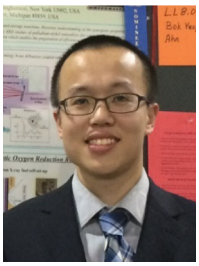

Shiyao Shan received his Ph.D in Chemistry at the State University of New York at Binghamton in 2016 under the supervision of Prof. Zhong. He is currently a postdoctoral scientist. He has co-authored many peer-reviewed papers and has two patent applications pending. His research interests include design, synthesis, characterization and application of nanoscale materials in cutting-edge technological areas such as clean energy production, conversion and storage, emission control, and chemical/biological sensing.

Haval Kareem is a Ph.D. candidate in the Chemistry Department at the State University of New York at Binghamton under the supervision of Prof. Zhong. He received his bachelor's degree of Chemistry in Baghdad University in 2002. His current research interests include design, synthesis and characterization of robust, active, and low-cost nanoparticle catalysts for reactions related to clean energy conversion technologies.

Jin Luo is a senior scientist at the State University of New York at Binghamton and an active entrepreneur at NSC Technology and FlexSurface. His research interests involve interfacial electrochemistry, catalysis, sensors, and nanoscale chemistry. Currently he has focused on developing advanced nanomaterials for applications in fuel cells, batteries, chemical sensors, and biomedical devices. He has co-authored many papers in peer-reviewed journals and is a co-inventor of a number of US Patents.

Chuan-Jian Zhong is a Professor of Chemistry and Materials Science at the State University of New York at Binghamton. He has many years of research experience in interdisciplinary areas of materials and analytical chemistry, focusing on design of functional nanomaterials for sustainable energy production, conversion and storage, and sensors for chemical and biological detection. He has published more than 280 peer-reviewed research articles, and is an inventor of about 20 US patents.

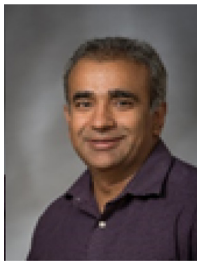

Sarvjit Shastri (B.S., Caltech; Ph.D., Cornell, 1994) is a physicist at the Advanced Photon Source at Argonne National Laboratory, primarily developing high-energy (50–150 keV) x-ray optics and scattering techniques. He has also worked on optics simulations for short-pulsed x-ray sources such as SASE- and seeded-XFELS.

Peter Kenesei is a physicist (M.Sc. Eotvos University, Ph.D. Eotvos University, 2010) at the Materials Physics and Engineering Group at the Advanced Photon Source at Argonne National Laboratory. He works on the development of high-energy x-ray diffraction microscopy and microtomography techniques. He has co-authored 80 publications in peer-reviewed journals. His current research interests include elastic and plastic deformation, damage and fatigue of complex material systems (composites, multilayers, biomaterials, batteries, fuel cells), high precision metrology, and computational materials science.